Engineering high charge transfer n-doping of graphene electrodes and its application to organic electronics

Simon Sanders[†], Andrea Cabrero-Vilatela[‡], Piran R. Kidambi[‡*], Jack A. Alexander-Webber[‡], Christ Weijtens[†], Philipp Braeuninger,[‡] Adrianus I. Aria,[‡] Malik M. Qasim,[‡] Timothy D. Wilkinson,[‡] John Robertson[‡], Stephan Hofmann[‡] and Jens Meyer[†]

[†]*Philips Research, Philipsstrasse 8, 52068 Aachen, Germany*

[‡]*Department of Engineering, University of Cambridge, 9 JJ Thomson Avenue, Cambridge CB3 0FA, UK*

[*]*Department of Mechanical Engineering, Massachusetts Institute of Technology, 77 Massachusetts Avenue, Cambridge, MA, USA*

ABSTRACT

Using thermally evaporated cesium carbonate (Cs_2CO_3) in an organic matrix, we present a novel strategy for efficient n-doping of monolayer graphene and a ~90% reduction in its sheet resistance to ~250 Ohm/sq. Photoemission spectroscopy confirms the presence of a large interface dipole of ~0.9 eV between graphene and the Cs_2CO_3/organic matrix. This leads to a strong charge transfer based doping of graphene with a Fermi level shift of ~1.0 eV. Using this approach we demonstrate efficient, standard industrial manufacturing process compatible graphene-based inverted organic light emitting diodes on glass and flexible substrates with efficiencies comparable to those of state-of-the-art ITO based devices.

INTRODUCTION

Atomically thin graphene films offer a unique combination of properties including high carrier mobilities, optical transparency, chemical inertness, flexibility and mechanical robustness, which make them highly interesting as transparent conductor (TC) material to enable novel form factors and device architectures for a range of applications including organic photovoltaic cells and organic light emitting diodes (OLEDs).[1–8] Most of these applications require low sheet resistances and detailed band engineering to optimize charge injection/extraction.[1–8] Hence effective doping and the controlled adjustment of the Fermi level are of crucial importance.[7–9] This is best achieved by charge transfer[7–9] or field-effect/electrostatic doping approaches,[10–12] as substitutional doping and other methods based on covalent bonding degrade the graphitic layer quality.[13–15] Numerous graphene doping schemes have been reported[16–22] including charge transfer from metal oxide,[7–9] molecular films and chemical doping via e.g. nitric acid (HNO_3)[20–22] or iron chloride ($FeCl_3$)[23]. Whereas these strategies work well for p-type doping of graphene, efficient n-type doping is much more challenging as the latter requires materials/molecular species with a very low work function which are hence prone to oxidation.[13–15,21,24–26] This challenge of n-doping is well-known in the field of organic electronics[27] and is compounded by the lack of a detailed understanding of doping mechanisms in complex interfaces.[28–30] Hence, the n-doping approaches and achievable doping efficiencies for graphene are of high relevance not only to applications but also as a model system to develop a detailed understanding of the n-doping mechanisms for organic electronics in general.

Here, we focus on the n-type doping of monolayer graphene with an alkali metal compound i.e. cesium carbonate (Cs_2CO_3). Alkali metals are well known for their efficient electron transfer in organic semiconductors and their compounds are typically used for ease of material handling and process control.[28,29,31] By embedding Cs_2CO_3 in a bathophenanthroline (Bphen) matrix we develop a highly efficient n-type doping strategy for graphene that allows us to demonstrate inverted OLEDs on glass and plastic substrates with device characteristics that can compete with those of state-of-the-art indium tin oxide (ITO) based OLEDs. We show that the graphene n-doping thereby achieved is significantly higher than for recently reported polymer films containing aliphatic amine groups,[26] polyethylenimine ethoxylated (PEIE),[26,27,32] and using photoemission spectroscopy we develop a detailed understanding of the doping mechanism and energy level alignment.

RESULTS

Fig. 1a shows the change in sheet resistance measured in-situ for a graphene monolayer during Cs_2CO_3 deposition by evaporation. The sheet resistance is first measured in air and then in vacuum. The slight increase in sheet resistance at lower pressures (around 10^{-6} mbar) is attributed to a diminishing unintentional p-doping due to air exposure[7–9] and PMMA residue from the graphene transfer process.[33–35] The following evaporation of a few Angstrom (1-2Å) of Cs_2CO_3 leads to a rapid sheet resistance increase from ~1300 to ~2500 Ohm/sq. At first view this might be contradictory to an effective n-doping, however, the graphene remains in vacuum unintentionally p-doped. Thus, the first deposited Cs_2CO_3 molecules compensate the p-doping, shifting the Fermi level towards the Dirac Point. At this point the density of states (DOS) has a minimum resulting in corresponding a sheet resistance maximum. With increasing deposition the sheet resistance drops rapidly and reaches ~250 Ohm/sq at a Cs_2CO_3 thickness of ~10Å. The very efficient n-doping is caused by the large work function difference of Cs_2CO_3 and graphene (see UPS/XPS in Fig. 3 below) inducing a strong charge transfer doping.[28,29] We will discuss this further in detail. Hartwigsen et al.[31] have studied the charge transfer in alkali-graphite intercalation compounds and identified that the 6s electrons of caesium atoms can fill the π* states of graphite which leads to n-doping.
Complete removal of all un-intentional p-doping (including any PMMA residuals and atmospheric contamination) requires cleaning procedures, such as annealing in an Ar/H_2 mixture at elevated temperature > 300°C, which can damage the graphene and induce defects.[33] A simple alternative to compensate the initial graphene p-doping and to allow a more detailed analysis of the extent of n-doping by Cs_2CO_3 is to electrostatically gate graphene by applying an external electric field that shifts the Fermi level to the Dirac Point.[36] By applying a gate voltage V_g between 0 and 50V to the backside of the Si wafer support (see inset of Fig. 1a) we shift the Fermi level towards the Dirac Point thereby increasing the sheet resistance, as shown in Fig. 1b. A maximum sheet resistance ~5-5.5 kOhm/sq is found at a gate voltage of ~ 45V with some variation between samples, which corresponds well with the theoretical sheet resistance of intrinsic graphene of ~6 kOhm/sq.[2] From this we estimate that the initial unintentional p-doping of as-loaded graphene results in a hole concentration given approximately by $n = C_g V_g/e = 3.3\times10^{12}$ cm^{-2}, where C_g[300nm SiO_2] = 11.6nF/cm^2 and V_g=45V, leading to a Fermi level of 210meV below the Dirac Point. By increasing the gate voltage to V_g>45V a decrease in sheet resistance is observed. However, at voltages beyond 50V we noticed interfering parasitic effects that hampered the measuring of the full Fermi Dirac characteristic. For the sake of completeness the extrapolated Fermi Dirac shape up to higher voltages is shown in the inset of Fig. 1b. The sheet resistance of monolayer graphene in this case

is ~5.5 kOhm/sq. The initial sheet resistance during the deposition of the first few Angstroms of Cs_2CO_3 suggests the Fermi level of the initially p-doped graphene is moved close to the Dirac Point due to gating (Fig.1b). However, both samples, with and without applied gate voltage, show similar final sheet resistance values. Hence, our results indicate that due to the substantial shift in the Fermi level induced by Cs_2CO_3 doping, which we describe below, the slight initial p-doping has only a negligible effect on the absolute sheet resistance values obtainable with Cs_2CO_3 doping.

While the doping efficiency of Cs_2CO_3 is high, the doping stability and device integration of such a very thin, highly reactive layer is non-trivial. Bphen is often used as electron transport material in organic devices and has a lowest unoccupied molecular orbital (LUMO) of ~2.4eV and highest occupied molecular orbital (HOMO) of ~6.5eV.[28,29]

Since the LUMO of Bphen lies energetically lower than the WF of Cs_2CO_3 (~1.8eV)[x] by co-evaporation the organic material can be effectively n-doped by charge transfer as shown in Fig. 2 while simultaneously increasing the doping stability.[x,] We note that there are reports in literature showing that Cs2CO3 decomposes to cesium oxide during thermal evaporation, thus the given WF might corresponds to CsOx.

We found an optimum Cs_2CO_3 doping concentration of around 10 vol.% (see Fig. S1 in Supplementary Information). The current voltage characteristics of two single carrier devices comprised of a 100 nm Cs_2CO_3 doped and un-doped Bphen layer sandwiched between ITO and an Al electrode is shown in Fig. 2a. A significantly improved conductivity of more than eight orders of magnitude due to Cs_2CO_3 doping is observed, consistent with previous literature.[29] Further, Cs_2CO_3 can not only efficiently dope Bphen, but at the same time it can also dope graphene. This is demonstrated in Fig. 2b where a co-evaporated Bphen:Cs_2CO_3 (10 vol%) leads to a significant sheet resistance reduction. The relative changes are very similar to a Cs_2CO_3 layer (Fig. 1), but a thicker layer of 50-70Å is needed (Fig. 2) to obtain a comparable doping efficiency to Fig. 1. The sheet resistance of graphene does not change due to the deposition of only a Bphen layer confirming that the doping is primarily due to Cs_2CO_3. Our n-doped graphene layer (monolayer with 10nm Bphen:Cs_2CO_3) shows a very high transmittance of around ~96% across the visible part of the spectrum (see supplementary information Fig. S2). Thus, the doping layer has only a minor effect on the overall transparency of our graphene electrode.

The key advantage of embedding Cs_2CO_3 in a Bphen matrix by co-evaporation is the higher doping stability as shown in Fig. 2c. Here two samples of graphene doped either with Cs_2CO_3 ~~and~~ Bphen:Cs_2CO_3 mixture are stored for 30min in vacuum at a base pressure of around 10^{-6} mbar and then in N_2 (see Fig. 2c). While the changes in vacuum are almost negligible for both samples, a

clear difference is seen in N_2. While the pure Cs_2CO_3 doping of graphene is almost completely eliminated due to N_2 exposure, the Cs_2CO_3 in a Bphen matrix merely shows an increase in sheet resistance of ~20%. N_2 itself is fairly non-reactive but trace amounts of residual gasses e.g. water vapor, oxygen etc. in the N_2 atmosphere could potentially oxidize the highly reactive Cs_2CO_3 layer. A combination of complementary ultraviolet photoelectron spectroscopy (UPS) and X-ray photoelectron spectroscopy (XPS) is used to elucidate the n-doping mechanism. Fig. 3a shows the UPS spectra plotted with respect to the Fermi level of graphene and thin layers of Bphen:Cs_2CO_3 (2, 6, 12 and 25Å) on top. The photoemission onset (left graph, marked with black lines) of graphene is measured at an energy of ~16.63eV. By subtracting the excitation energy (He Iα source with 21.22eV) the WF of graphene can be determined as ~4.59eV (here still unintentionally p-doped). Upon deposition of a few Angstrom of Bphen:Cs_2CO_3 (6Å) the photoemission onset shifts rapidly by ~1.9eV towards higher binding energies which corresponds to a lowering of the WF and can be attributed to a strong interface dipole. With further incremental deposition from 6 to 25Å only a very small additional shift of around 0.2eV is found resulting in a final Bphen:Cs_2CO_3 WF of ~2.4eV. Looking at the valence band states (right graph in Fig. 3a), the graphene spectra show a low DOS extending up to the Fermi level, as expected for the semimetal. The HOMO edge of Bphen:Cs_2CO_3 (marked with black lines) shifts strongly within the first few Angstrom, but then almost saturates at a thickness of around 12-25Å. The very small shifts of ~0.2 eV from thicknesses of 6 Å onwards suggest a very small downwards band bending with respect to the Fermi level. At a thickness of 25Å the HOMO edge of Bphen:Cs_2CO_3 is ~4.28eV below the Fermi levels corresponding to an ionisation energy (IE) of ~6.8eV that is in good agreement to previous reports.[37] Considering ~~an~~ Bphen:Cs_2CO_3 electron affinity of ~2.4eV, as measured by Meyer et al.[37] via inverse photoelectron spectroscopy, the Fermi level can be determined to be only ~0.1eV below the LUMO level which clearly indicates the highly n-doped efficiency of our Bphen:Cs_2CO_3 layer.

Furthermore we used XPS analysis to probe the core level signatures at the graphene/ Bphen:Cs_2CO_3 interface, with the evolution of C 1s core levels plotted for incrementally increased n-doped organic layer thickness, see Fig. 3b. Since the information depth of our XPS source [Mg (Kα) radiation with 1253.6eV] is larger compared to the UPS measurements, the method allows for probing the Fermi level shift of graphene caused by the dopant. The C1s core level signature of graphene features one distinct peak at 284.7eV (purple color) that can be attributed to the C-C bond and a second small peak (green color) at around 285.8eV that can be assigned to C-O defect states.[7] Upon deposition of Bphen:Cs_2CO_3 the characteristic C1s graphene peak shifts by ~1eV

towards higher binding energies and an additional peak from the organic electron transport material is seen. The large shift is a clear indication of n-doping of graphene[38,39] shifting the Fermi level from the valance band of our as-loaded unintentionally p-doped graphene into the conduction band, as illustrated in Fig. 3c. Interestingly, the shift takes place within the deposition of the first 2 to 6Å of Bphen:Cs_2CO_3 indicating a very efficient charge transfer doping. Assuming a Fermi level position of as-loaded p-doped graphene of ~0.2eV below the Dirac Point, as discussed above, the total shift into the conduction band is ~0.8eV, hence more effective than the n-doping by PEIE (see discussion below) and the charge transfer p-doping with metal oxide (MoO_3) where a shift of ~0.55eV from the Dirac Point into the valence band was identified (taking into account the same unintentionally p-doping of 0.2 eV).[7–9,40] While the UPS spectra show a strong interface dipole at the graphene / Bphen:Cs_2CO_3 interface, the XPS C1s core levels (Fig. 3b) reveals a concurrent shift to higher binding energies by ~1 eV indicating not only a charge transfer based n-doping of graphene, but also, as a consequence, a lowering of the WF from ~4.6eV to ~3.6eV. Fig. 3d summarizes the observed energy level alignment at the graphene / Bphen:Cs_2CO_3 interface. Based on the combined UPS/XPS analysis a resulting interfacial dipole of 0.9eV arises which nearly aligns the transport levels of graphene and Bphen:Cs_2CO_3. Hence the barrier for electron injection is very low.

Fig. 4a shows the Raman spectra of monolayer CVD graphene directly after transfer, compared with Bphen:Cs_2CO_3 and PEIE doped graphene, respectively, prepared using the technique described in Reference [26]. A clear systematic shift is observed in the G peak (~1600 cm^{-1}) position where the energy of the G-band phonon of the doped graphene samples increases with respect to the unintentionally doped control sample. The G-band shift for PEIE doped graphene is also larger than reported in literature[26,32] however, still significantly lower compared to Bphen:Cs_2CO_3. The theoretical dependence of the Raman G-band shift as a function of doping (Fermi energy) is given in Fig. 4b.[41,42] By comparing the measured shifts with respect to un-doped graphene we can estimate the doping levels within the graphene. We extract a hole density of $2.1\pm0.3\times10^{12}$ cm^{-2}, for the unintentionally p-doped graphene in good agreement with the field effect electrical transport data described above. We find an electron density of $n = 1.3 \pm 0.1\times10^{13}$ cm^{-2} and $2.2 \pm 0.2\times10^{13}$ cm^{-2}, for PEIE and Bphen:Cs_2CO_3 doped graphene respectively, showing that the BPhen:Cs_2CO_3 is significantly more effective than PEIE as a dopant. The Raman data suggest a large Fermi energy shift $\Delta E_F > 800$ meV due to Bphen:Cs_2CO_3 doping, in good agreement with the XPS data described above (Fig. 3).

The effective n-doping allows for the fabrication of graphene-based inverted OLED structures, where the doped graphene forms the bottom contact (see Fig. 5a). This architecture opens up higher device stability as well as the integration of n-channel transistors for high resolution Active-Matrix displays. First we evaluate devices based on monolayer CVD-graphene transferred onto glass substrates. As shown in the inset of Fig. 5a, the inverted OLED stack starts with a co-evaporation of a Bphen:Cs_2CO_3 layer. This multifunctional layer induces strong n-doping of graphene, as well as efficient charge carrier injection and transport. In addition, the high conductivity (see Fig. 2a) and low absorption of Bphen:Cs_2CO_3 allow for the use of a relatively thick layer in the OLED stacks without deteriorating the electro-optical performance. We introduced a 115nm thick Cs_2CO_3 doped Bphen layer in our OLED architecture to smoothen contamination and wrinkles on the graphene samples which are predominantly caused by the transfer process. Further details of the OLED stack fabrication are given in the experimental section. Fig. 5 a,b compare the characteristics of a graphene-based OLED and an ITO reference device both fabricated in the same process, thus comprising identical organic layer stacks with a thick n-doped injection layer. The devices show similar luminance/current voltage characteristics with an on-set voltage of around 3V and high lumen outputs of 3000cd/m² at 6V.

A closer look at the data reveals that the graphene-based OLED reaches a higher luminance at a given voltage which we attribute to lower optical losses of the electrode material. This can be more clearly seen in the efficiency plots of Fig. 5b. At a typical luminance of 1000cd/m² the ITO based OLED has a current efficiency of 37cd/A compared to 40cd/A for the graphene-based OLED. Organic devices are very sensitive to oxygen and moisture and therefore need an encapsulation which protects them from environmental conditions. As our n-doped graphene layer shows a high stability under inert conditions, see Fig. 2, we expect reliable OLED operation with our n-doped graphene electrode.

Finally, we fabricate and evaluate graphene-based inverted OLED structures on flexible plastic substrates. The challenge of using thin flexible plastic substrates, like polyethylene terephthalate (PET) or polyethylennaphthalate (PEN) are a) high surface roughness (rms > 50nm) which can easily short thin film devices and b) high temperature intolerance (typically for >150°C). Often PEDOT:PSS is used as planarization layer for graphene on plastic foils, despite the acidic nature of its aqueous dispersion which can significantly decrease the device lifetime. Here, we avoid using PEDOT:PSS and instead coat the PEN foil with SU8 photoresist to planarize them. Then graphene is transferred followed by the deposition of the inverted OLED stack (see experimental methods). We emphasize that standard ITO on glass is typically sputtered and annealed at 250°C to reach low sheet resistance values and a high optical transmittance. On the other hand, ITO on plastic foil cannot

be post-treated at elevated temperatures because of the limited temperature stability of the PEN. This temperature constraint also limits the post-transfer annealing steps to clean the graphene surface of polymer residue on flexible plastic substrates. To overcome these constraints we re-design our n-doped graphene-based OLED stack and graphene transfer procedure (see experimental section) to achieve performance comparable to a sputtered and subsequently annealed state-of-the-art ITO-based device on rigid glass substrates (Fig. 5c), albeit at slightly lower overall power efficiencies. At high luminance values of 3000 cd/m² both OLEDs, ITO on glass and graphene on PEN foil, achieved a similar power efficiency of 10 lm/W. The advent of cleaner graphene transfer procedures is an area of active research and is further expected to alleviate these constraints allowing for greater power efficiencies in flexible OLEDs using our novel n-doping approach and inverted stack design.

CONCLUSIONS

In conclusion, we demonstrate a strategy to efficiently n-dope graphene by a simple co-evaporation of Bphen:Cs_2CO_3. Complementary in-situ sheet resistance measurements, XPS, UPS and Raman allow for a detailed understanding of the charge transfer based n-doping mechanism. The co-evaporation of Bphen:Cs_2CO_3 not only lowers the graphene sheet resistance of monolayer graphene by one order of magnitude, but also allows efficient electron injection in inverted OLEDs. The as-fabricated OLEDs on glass as well as flexible substrates have efficiencies comparable to state-of-the-art ITO electrodes. We expect the developed understanding and doping process strategy to be relevant to numerous applications that utilize graphene-based electrodes or use electrodes based on carbon nanotubes or related other nanomaterials.

EXPERIMENTAL METHODS

Monolayer graphene (MLG) synthesis was performed on Cu foils (Alfa Aesar Puratronic, 99.999% purity, 25 µm thick) using a low-pressure chemical vapor deposition process (LPCVD) described in detail elsewhere.[38,39,43] The synthesized graphene was transferred using a carrier layer, poly (methyl methacrylate) (PMMA 495K diluted to 2% in Anisole)[44] while 0.1 M aqueous solution of $(NH_4)_2S_2O_8$ was used to etch the Cu foil. The MLG-PMMA stack was transferred to the desired substrate (SiO_2 (300 nm)/Si or glass substrates i.e. SiO_2 1.4 mm thick) after multiples rinses in DI water and dried.[35,45] The carrier layer was finally dissolved using acetone followed by isopropanol and blow dried in nitrogen. An anneal in 4 mbar H_2 at ~300 °C for 60 minutes was performed to remove residual PMMA post transfer.

MLG transferred onto flexible substrates was carried out using polystyrene (PS diluted in toluene [0.08g/ml]) as a support layer. Cu catalyst was etched with an aqueous solution of $FeCl_3$ 0.5M followed by a bath in HCl (37%). Graphene/PS layer was then rinsed in DI water and transferred onto PEN+SU8 substrates. Polystyrene was finally dissolved using ethyl acetate followed by an IPA bath and N_2 dry.

All organic and inorganic layers were prepared by thermal evaporation in a custom-build deposition system at a base pressure of 10^{-6} mbar. As substrates we used cleaned ITO pre-coated glass and graphene transferred on glass, respectively. The OLED stack comprises the following layer sequence: 115nm Bphen:Cs_2CO_3 (10 vol%), 20 nm 1,3,5-tris-phenyl-2-benzimidazolyl-benzene (TPBi), 15nm TBPi doped with the green phosphorescent emitter materials with bis(2-phenylpyridine)(acetylacetonate)iridium(III) [$Ir(ppy)_2(acac)$] (10 vol%), 55nm 4,4'-Bis(*N*-carbazolyl)-1,1'-biphenyl (CBP), 5nm MoO_3, and 100nm Aluminum. For the graphene OLED on plastic foil and the control device a two-fold OLED stack was used employing the same functional layers as described above, but with an intermediate charge generation layer comprised of a Bphen:Cs_2CO_3 and MoO3 doped CBP layer.

For the in-situ sheet resistance measurements we used a 4-point probe setup which was integrated in the custom-build vacuum deposition system. The Cs_2CO_3 and Bphen:Cs_2CO_3 layers were evaporated with a deposition rate of 0.05-0.5 Å/sec on the graphene samples and the change of sheet resistance was monitored.

The photoelectron spectroscopy studies (XPS and UPS) were performed in a multi-chamber VG Microlab 300 A ESCA system with a base pressure of around 10^{-8} Pa.[7,9] An x-ray source with a Mg (Kα) radiation was used for XPS and a differentially pumped, windowless discharge lamp was utilized to conduct UPS measuremnts.[7,9] The UPS spectra were taken using He–I radiation. The IE was determined from the energetic difference in the UPS spectrum between the onset of photoemission and the valence band edge of the metal oxide films. The work function WF was derived from the onset of photoemission in combination with the known position of the Fermi energy.[7,9]

Raman spectroscopy was performed using a Renishaw CCD detector with a 532nm laser excitation wavelength. Spectra for the PEIE and unintentionally doped samples were taken using a top-side geometry. The Bphen:Cs_2CO_3 doped graphene were taken with a back-side excitation through the glass substrate, where the graphene Raman spectrum was obtained by taking the spectrum for Bphen:Cs_2CO_3 doped graphene and subtracting a reference spectrum of pure Bphen:Cs_2CO_3 taken on the same sample.

ACKNOWLEDGEMENTS

Funding via EU FP7 programme Grafol (Grant No. 285275) and EPSRC programme GRAPHTED (Grant No. EP/K016636/1) is acknowledged. P.R.K. acknowledges the Lindemann Trust Fellowship. J.A.A.-W. acknowledges a Research Fellowship from Churchill College, Cambridge. A.C.V. acknowledges the Conacyt Cambridge Scholarship and Roberto Rocca Fellowship.

REFERENCES

1 R. G. Gordon, *MRS Bull.*, 2000, 52–57.

2 K. S. Novoselov, V. I. Fal'ko, L. Colombo, P. R. Gellert, M. G. Schwab and K. Kim, *Nature*, 2012, **490**, 192–200.

3 J. Hwang, H. Kyw Choi, J. Moon, T. Yong Kim, J.-W. Shin, C. Woong Joo, J.-H. Han, D.-H. Cho, J. Woo Huh, S.-Y. Choi, J.-I. Lee and H. Yong Chu, *Appl. Phys. Lett.*, 2012, **100**, 133304.

4 N. Li, S. Oida, G. S. Tulevski, S.-J. Han, J. B. Hannon, D. K. Sadana and T.-C. Chen, *Nat. Commun.*, 2013, **4**, 2294.

5 Y. Wang, X. Chen, Y. Zhong, F. Zhu and K. P. Loh, *Appl. Phys. Lett.*, 2009, **95**, 063302.

6 J. Wu, M. Agrawal, H. A. Becerril, Z. Bao, Z. Liu, Y. Chen and P. Peumans, *ACS Nano*, 2010, **4**, 43–8.

7 J. Meyer, P. R. Kidambi, B. C. Bayer, C. Weijtens, A. Kuhn, A. Centeno, A. Pesquera, A. Zurutuza, J. Robertson and S. Hofmann, *Sci. Rep.*, 2014, **4**, 5380.

8 A. Kuruvila, P. R. Kidambi, J. Kling, J. B. Wagner, J. Robertson, S. Hofmann and J. Meyer, *J. Mater. Chem. C*, 2014, **2**, 6940.

9 P. R. Kidambi, C. Weijtens, J. Robertson, S. Hofmann and J. Meyer, *Appl. Phys. Lett.*, 2015.

10 T.-J. Ha, K. Chen, S. Chuang, K. M. Yu, D. Kiriya and A. Javey, *Nano Lett.*, 2015, **15**, 392–7.

11 J. H. J. Ostrowski and J. D. Eaves, *J. Phys. Chem. B*, 2014.

12 Y. Zhang, T. Tang, C. Girit, Z. Hao, M. C. Martin, A. Zettl, M. F. Crommie, Y. R. Shen and F. Wang, *Nature*, 2009, **459**, 820–823.

13 B. Guo, Q. Liu, E. Chen, H. Zhu, L. Fang and J. R. Gong, *Nano Lett.*, 2010, **10**, 4975–80.

14 R. J. Nicholls, A. T. Murdock, J. Tsang, J. Britton, T. J. Pennycook, A. Koós, P. D. Nellist, N. Grobert and J. R. Yates, *ACS Nano*, 2013, **7**, 7145–7150.

15 M. Xu, T. Liang, M. Shi and H. Chen, *Chem. Rev.*, 2013, **113**, 3766–98.

16 T. Sun, Z. L. Wang, Z. J. Shi, G. Z. Ran, W. J. Xu, Z. Y. Wang, Y. Z. Li, L. Dai and G. G. Qin, *Appl. Phys. Lett.*, 2010, **96**, 133301.

17 H. Park, P. R. Brown, V. Bulović and J. Kong, *Nano Lett.*, 2012, **12**, 133–140.

18 T.-H. Han, Y. Lee, M.-R. Choi, S.-H. Woo, S.-H. Bae, B. H. Hong, J.-H. Ahn and T.-W. Lee, *Nat. Photonics*, 2012, **6**, 105–110.

19 Y. Wang, S. W. Tong, X. F. Xu, B. Ozyilmaz and K. P. Loh, *Adv. Mater.*, 2011, **23**, 1514–8.

20 S. Bae, H. Kim, Y. Lee, X. Xu, J. Park, Y. Zheng, J. Balakrishnan, T. Lei, H. R. Kim, Y. Il Song, Y.-J. Kim, K. S. Kim, B. Ozyilmaz, J.-H. Ahn, B. H. Hong and S. Iijima, *Nat. Nanotechnol.*, 2010, **5**, 574–8.

21 J. B. Bult, R. Crisp, C. L. Perkins and J. L. Blackburn, *ACS Nano*, 2013, **7**, 7251–61.

22 D.-Y. Wang, I. Huang, P. Ho, S. Li, Y. Yeh, D. Wang, W.-L. Chen, Y. Lee, Y. Chang, C.-C. Chen, C. Liang and C. Chen, *Adv. Mater.*, 2013, **25**, 4521–6.

23 I. Khrapach, F. Withers, T. H. Bointon, D. K. Polyushkin, W. L. Barnes, S. Russo and M. F. Craciun, *Adv. Mater.*, 2012, **24**, 2844–9.

24 D. Choudhury, B. Das, D. D. Sarma and C. N. R. Rao, *Chem. Phys. Lett.*, 2010, **497**, 66–69.

25 X. Wang, J. Bin Xu, W. Xie and J. Du, *J. Phys. Chem. C*, 2011, **115**, 7596–7602.

26 H. Sojoudi, J. Baltazar, L. Tolbert, C. Henderson and S. Graham, *Adv. Mater. Interfaces*, 2014, **1**.

27 Y. Zhou, C. Fuentes-Hernandez, J. Shim, J. Meyer, A. J. Giordano, H. Li, P. Winget, T. Papadopoulos, H. Cheun, J. Kim, M. Fenoll, A. Dindar, W. Haske, E. Najafabadi, T. M. Khan, H. Sojoudi, S. Barlow, S. Graham, J.-L. Brédas, S. R. Marder, A. Kahn and B. Kippelen, *Science*, 2012, **336**, 327–32.

28 J. Huang, Z. Xu and Y. Yang, *Adv. Funct. Mater.*, 2007, **17**, 1966–1973.

29 Y. Cai, H. X. Wei, J. Li, Q. Y. Bao, X. Zhao, S. T. Lee, Y. Q. Li and J. X. Tang, *Appl. Phys. Lett.*, 2011, **98**, 113304.

30 H.-Y. Park, J. Yoon, J. Jeon, J. Kim, S. Jo, H. Yu, S. Lee and J. Park, *Org. Electron.*, 2015, **22**, 117–121.

31 C. Hartwigsen, W. Witschel and E. Spohr, *Phys. Rev. B*, 1997, **55**, 4953–4959.

32 M.-J. Cha, W. Song, Y. Kim, D. S. Jung, M. W. Jung, S. Il Lee, P. D. Adhikari, K.-S. An and C.-Y. Park, *RSC Adv.*, 2014, **4**, 37849.

33 M. Kratzer, B. C. Bayer, P. R. Kidambi, Matković Aleksandar, Andrea Cabrero-Vilatela Robert S. Weatherup, C. Teichert and S. Hofmann, *Appl. Phys. Lett.*, 2015.

34 X.-T. Kong, A. A. Khan, P. R. Kidambi, S. Deng, A. K. Yetisen, B. Dlubak, P. Hiralal, Y. Montelongo, J. Bowen, S. Xavier, K. Jiang, G. A. J. Amaratunga, S. Hofmann, T. D. Wilkinson, Q. Dai and H. Butt, *ACS Photonics*, 2015, 150120150220004.

35 H. Butt, P. R. Kidambi, B. Dlubak, Y. Montelongo, A. Palani, G. A. J. Amaratunga, S. Hofmann and T. D. Wilkinson, *Adv. Opt. Mater.*, 2013, **1**, 869–874.

36 S. Badhwar, J. Sibik, P. R. Kidambi, H. E. Beere, J. Axel Zeitler, S. Hofmann and D. A. Ritchie, *Appl. Phys. Lett.*, 2013, **103**, 121110.

37 J. Meyer, M. Kröger, S. Hamwi, F. Gnam, T. Riedl, W. Kowalsky and A. Kahn, *Appl. Phys. Lett.*, 2010, **96**, 193302.

38 P. R. Kidambi, B. C. Bayer, R. Blume, Z.-J. Wang, C. Baehtz, R. S. Weatherup, M.-G. Willinger, R. Schloegl and S. Hofmann, *Nano Lett.*, 2013, **13**, 4769–78.

39 R. Blume, P. R. Kidambi, B. C. Bayer, R. S. Weatherup, Z.-J. Wang, G. Weinberg, M.-G. Willinger, M. Greiner, S. Hofmann, A. Knop-Gericke and R. Schlögl, *Phys. Chem. Chem. Phys.*, 2014, **16**, 25989–26003.

40 J. Meyer, S. Hamwi, M. Kröger, W. Kowalsky, T. Riedl and A. Kahn, *Adv. Mater.*, 2012, **24**, 5408–27.

41 A. Das, S. Pisana, B. Chakraborty, S. Piscanec, S. K. Saha, U. V Waghmare, K. S. Novoselov, H. R. Krishnamurthy, A. K. Geim, A. C. Ferrari and A. K. Sood, *Nat. Nanotechnol.*, 2008, **3**, 210–5.

42 A. C. Ferrari and D. M. Basko, *Nat. Nanotechnol.*, 2013, **8**, 235–46.

43 P. R. Kidambi, C. Ducati, B. Dlubak, D. Gardiner, R. S. Weatherup, M. Martin, P. Seneor, H. Coles and S. Hofmann, *J. Phys. Chem. C*, 2012, **116**, 22492–22501.

44 P. R. Kidambi, R. Blume, J. Kling, J. B. Wagner, C. Baehtz, R. S. Weatherup, R. Schloegl, B. C. Bayer and S. Hofmann, *Chem. Mater.*, 2014, **26**, 6380–6392.

45 R. Degl'Innocenti, D. S. Jessop, Y. D. Shah, J. Sibik, J. A. Zeitler, P. R. Kidambi, S. Hofmann, H. E. Beere and D. A. Ritchie, *ACS Nano*, 2014, **8**, 2548–54.

FIGURES

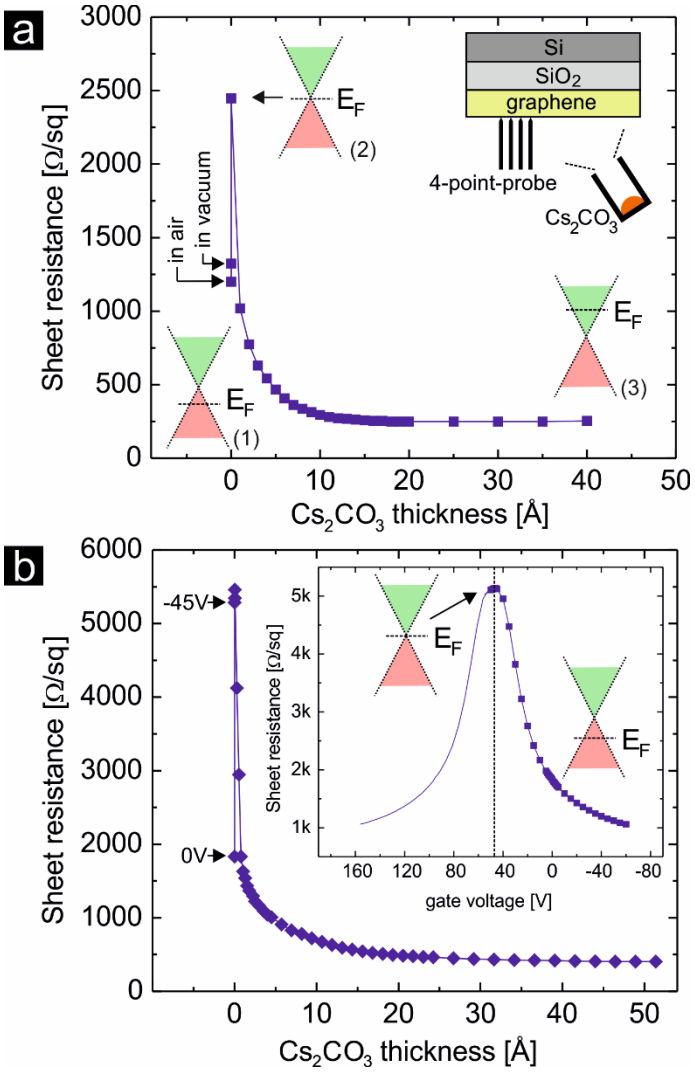

Figure 1: In-situ sheet resistance measurements of graphene during the deposition of thermal evaporated Cs_2CO_3 in vacuum. Fermi Dirac cones illustrating doping level at various positions_(1) as-loaded, unintentionally p-doped graphene, (2) compensated p-doping effect by Cs_2CO_3 doping and (3) highly Cs_2CO_3 n-doped graphene (a) Without applied gate voltage. Inset shows setup. (b) With applied gate voltage of 45V. Inset shows sheet resistance of unintentionally doped graphene with respect to applied gate voltage.

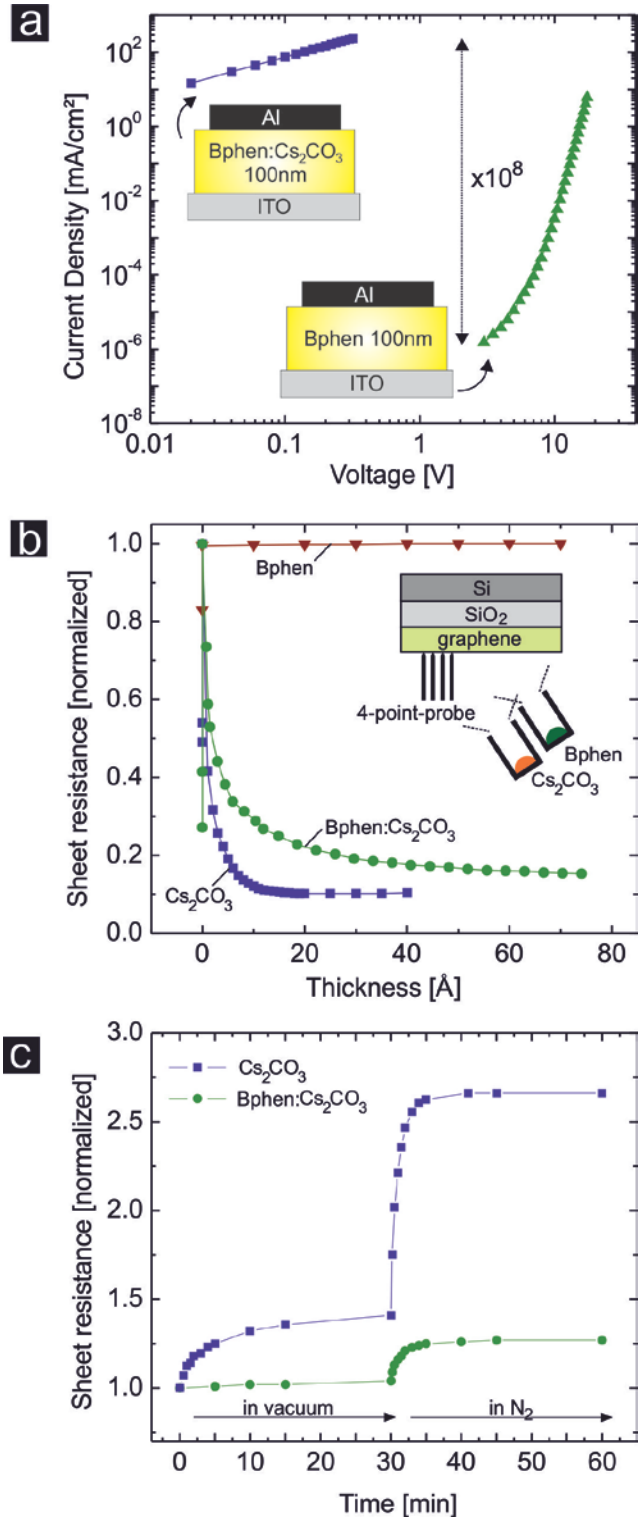

Figure 2(a): Current density voltage characteristics of single carrier devices with 100nm Bphen layer and 100nm Cs_2CO_3 doped Bphen layer. (b) In-situ sheet resistance measurements of graphene during the deposition of thermal evaporated Cs_2CO_3, Bphen and Cs_2CO_3 doped Bphen. (c) Sheet resistance of Cs_2CO_3 and Cs_2CO_3 doped Bphen upon storage in vacuum and N_2.

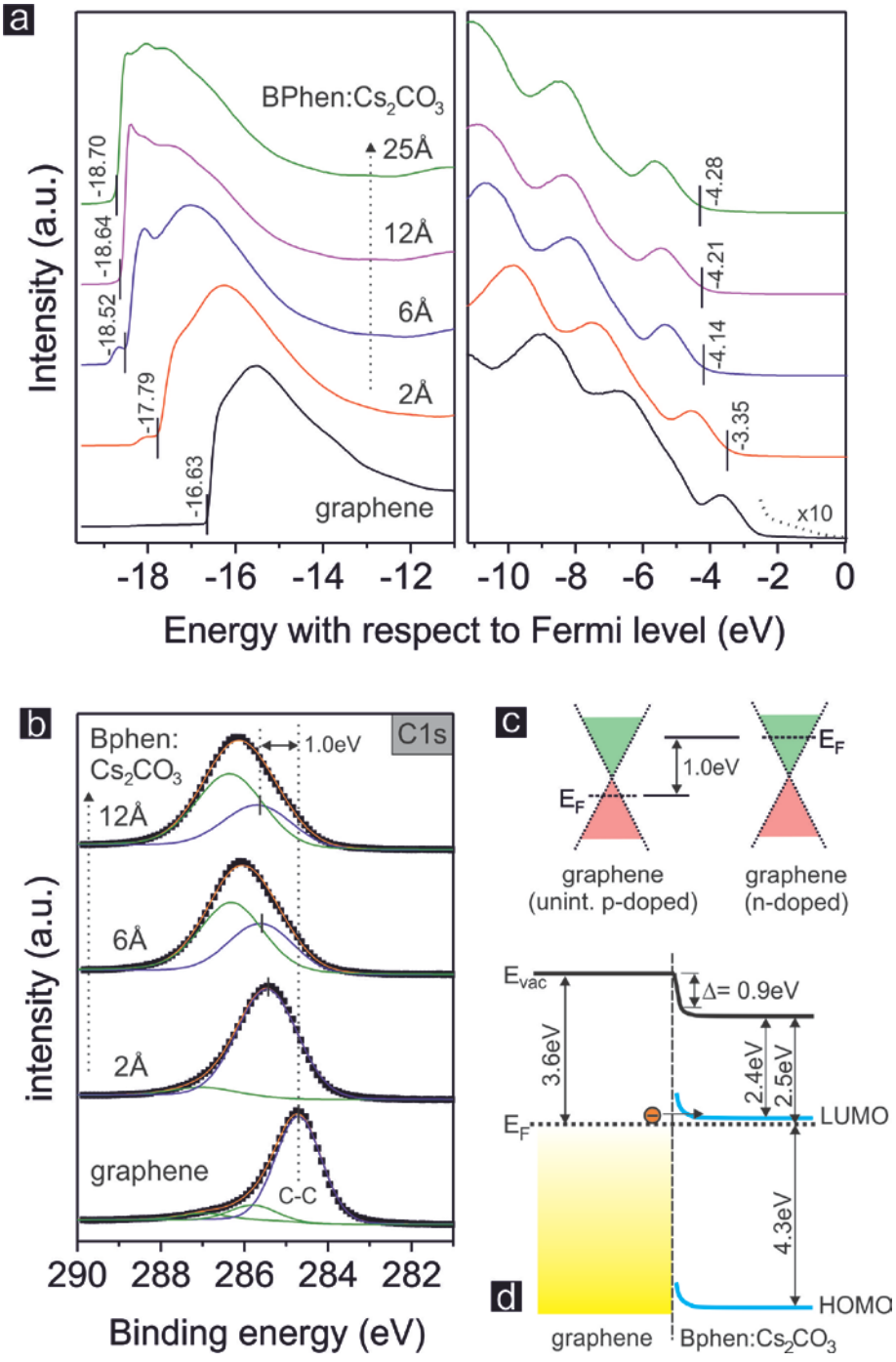

Figure 3(a): UPS spectra plotted with respect to Fermi level of monolayer graphene (initially unintentionally p-doped) with incrementally deposited Bphen:Cs_2CO_3 layers. Left graph: Magnified view of the photoemission cut-off. Right graph: Magnified view of the valence band states. Ticks mark the position of the cut-off and valence band edges. (b) XPS C1s spectra of monolayer graphene with incrementally increased Bphen:Cs_2CO_3 layer thickness. (c) Schematic of graphene Fermi-Dirac cone illustrating the Fermi level shift due to the charge transfer process from Bphen:Cs_2CO_3. (d) Energy level alignment of n-doped graphene and Bphen:Cs_2CO_3 interface.

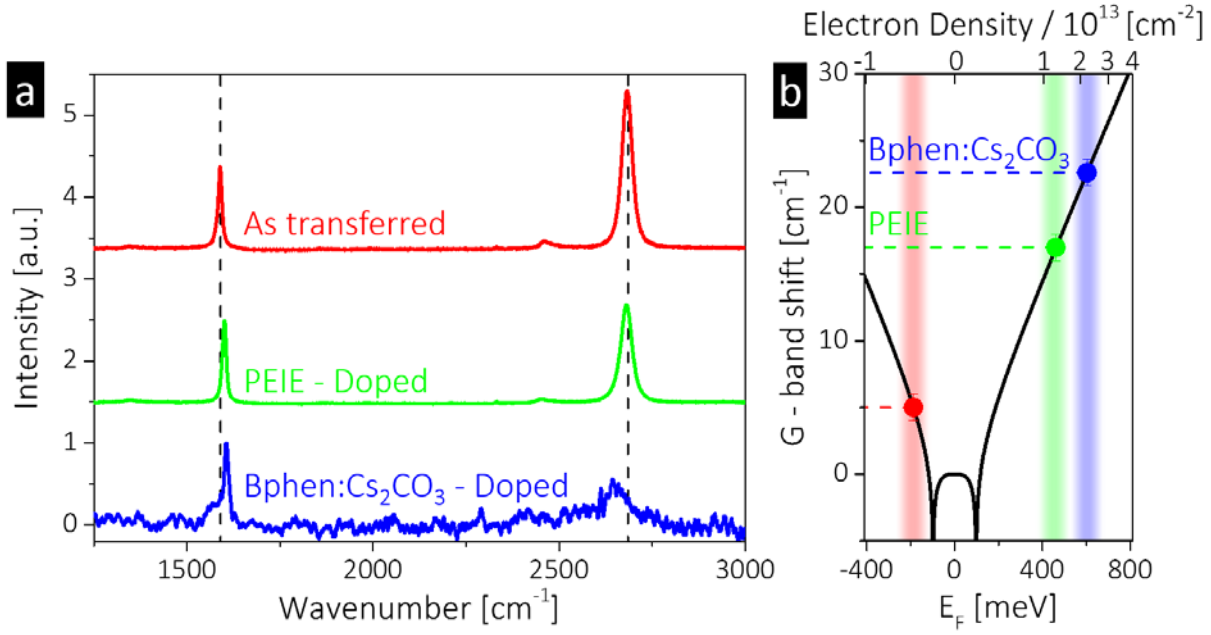

Figure 4(a): Raman spectra plotted for monolayer CVD graphene directly after transfer (red), and after doping with PEIE (green) and Bphen:Cs_2CO_3 (blue). The spectrum for Bphen:Cs_2CO_3 was background subtracted and measured through the transparent glass substrate, while the other spectra were measured from the top of the doping stack. (b) Theoretical dependence[41,42] of the Raman G-band shift as a function of doping (Fermi energy) from which we extract a hole density of $2.1\pm0.3\times10^{12}$ cm^{-2}, for the unintentionally p-doped graphene and an electron density of $n = 1.3\pm0.1 \times 10^{13}$ cm^{-2} and $2.2\pm0.2 \times 10^{13}$ cm^{-2}, for PEIE and Bphen:Cs_2CO_3 doped graphene respectively.

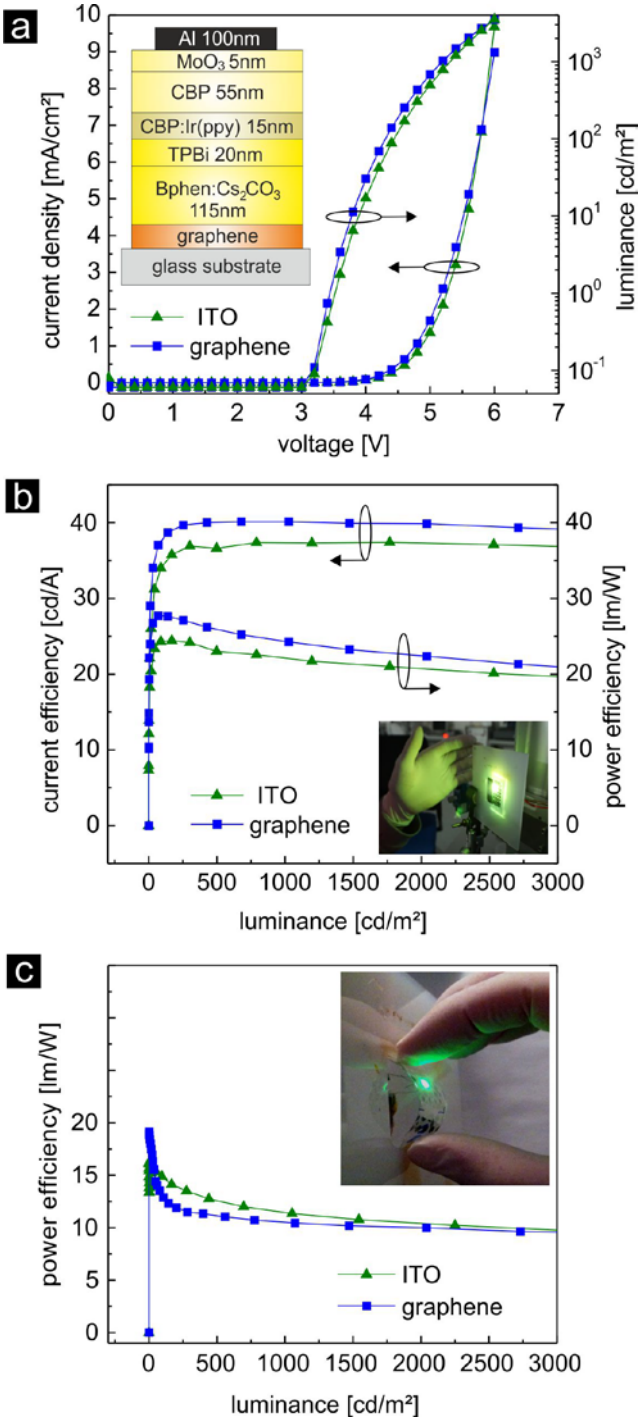

Figure 5: Device characteristics of OLEDs with either monolayer graphene or ITO electrode. (a) Current density and luminance versus voltage. Inset illustrates OLED layer stack comprising ITO or graphene bottom electrode and a Bphen:Cs_2CO_3 electron-injection layer. (b) Current and power efficiency versus luminance Inset shows photograph of powered MLG based OLED at high brightness level. (c) Power efficiency of OLEDs with either monolayer graphene on plastic foil or ITO on glass. Inset shows photograph of bended monolayer based OLED in on state.